C. R. Physique 17 (2016) 485–495

Contents lists available at ScienceDirect

Comptes Rendus Physique

www.sciencedirect.com

Condensed matter physics in the 21st century: The legacy of Jacques Friedel

A versatile lab-on-chip test platform to characterize elementary deformation mechanisms and electromechanical couplings in nanoscopic objects

Plate-forme versatile d'essai sur puce pour la caractérisation des mécanismes élémentaires de déformation et des couplages électromécaniques dans les objets nanoscopiques

Thomas Pardoen [a,*], Marie-Stéphane Colla [a], Hosni Idrissi [a,b], Behnam Amin-Ahmadi [b], Binjie Wang [b], Dominique Schryvers [b], Umesh K. Bhaskar [c], Jean-Pierre Raskin [c]

[a] *Institute of Mechanics, Materials and Civil Engineering, Université catholique de Louvain, Place Sainte Barbe, 2, B-1348 Louvain-la-Neuve, Belgium*
[b] *Electron Microscopy for Materials Science (EMAT), Department of Physics, University of Antwerp, Groenenborgerlaan, 171, B-2020 Antwerpen, Belgium*
[c] *Information and Communications Technologies, Electronics and Applied Mathematics (ICTEAM), Université catholique de Louvain, Place du Levant, 3, B-1348 Louvain-la-Neuve, Belgium*

ARTICLE INFO

Article history:
Available online 30 November 2015

Keywords:
Nanomechanical testing
Thin films
Size-effects
Fracture
In situ TEM
Piezoresistance

Mots-clés :
Essais nanomécaniques
Films minces
Effet de taille
Rupture
MET in situ
Piezoresistance

ABSTRACT

A nanomechanical on-chip test platform has recently been developed to deform under a variety of loading conditions freestanding thin films, ribbons and nanowires involving submicron dimensions. The lab-on-chip involves thousands of elementary test structures from which the elastic modulus, strength, strain hardening, fracture, creep properties can be extracted. The technique is amenable to in situ transmission electron microscopy (TEM) investigations to unravel the fundamental underlying deformation and fracture mechanisms that often lead to size-dependent effects in small-scale samples. The method allows addressing electrical and magnetic couplings as well in order to evaluate the impact of large mechanical stress levels on different solid-state physics phenomena. We had the chance to present this technique in details to Jacques Friedel in 2012 who, unsurprisingly, made a series of critical and very relevant suggestions. In the spirit of his legacy, the paper will address both mechanics of materials related phenomena and couplings with solids state physics issues.

© 2015 Académie des sciences. Published by Elsevier Masson SAS. All rights reserved.

RÉSUMÉ

Une plate-forme d'essai nanomécanique sur puce a été récemment développée afin de déformer, sous des conditions de chargement variées, des films minces, rubans et nanofils libres impliquant des dimensions submicroniques. Le laboratoire sur puce comprend des

* Corresponding author.
E-mail address: thomas.pardoen@uclouvain.be (T. Pardoen).

http://dx.doi.org/10.1016/j.crhy.2015.11.005
1631-0705/© 2015 Académie des sciences. Published by Elsevier Masson SAS. All rights reserved.

milliers de structures d'essai élémentaires à partir desquelles peuvent être extraits le module d'élasticité et les propriétés de résistance, d'écrouissage, de rupture et de fluage. La technique est adaptée pour des études in situ par microscopie électronique en transmission pour élucider les mécanismes sous-jacents fondamentaux de déformation et de rupture qui, souvent, induisent des effets de dépendance de la taille des échantillons. La méthode permet d'investiguer les couplages électriques et magnétiques ainsi que d'évaluer l'impact de niveaux de contrainte mécanique élevés sur divers phénomènes de physique de l'état solide. Nous avons eu la chance de pouvoir présenter cette technique à Jacques Friedel en 2012, lequel a, sans surprise, émis une série de suggestions critiques et particulièrement pertinentes. En hommage à son héritage scientifique, cet article aborde aussi bien des phénomènes relatifs à la mécanique des matériaux que des questions liées à des couplages en physique de l'état solide.

© 2015 Académie des sciences. Published by Elsevier Masson SAS. All rights reserved.

1. Introduction

The playground of solid-state physics has been enlarged in recent years owing to the development of novel nanomechanical testing set-ups that allow deforming nano-sized material systems, under controlled mechanical loads with additional electrical, magnetic or environmental effects, sometimes involving in situ characterization capabilities, see, e.g., reviews [1–4]. The most widely used methods in nanomechanics involve (see the review papers [1–4] and references therein) the following techniques: (i) nanoindentation consists in penetrating a hard sharp tip inside the material with continuous measurement of the load and displacement allowing to probe the response of volume elements with a characteristic dimension typically larger than 20 nm; (ii) AFM and its variants are used to probe (visco-)elastic and adhesion properties, of soft to medium soft systems, at even smaller length scales; (iii) micro- or nano-pillars compression, for instance with a flat nanoindentor tip, allows testing freestanding submicron specimens up to large strains but with the difficulty to produce clean samples with sharp geometrical tolerances; (iv) "wafer curvature" methods for thin films and coatings deposited on perfectly flat substrates and loaded through thermal expansion mismatch are particularly simple to operate to address the small strain response, though under the constraint of the underlying substrate; (v) various "top-down" tensile testing set ups consist of miniaturized version of macroscopic machines with the difficulty to manipulate micrometer-sized samples and to apply and measure extremely small loads and displacements; (vi) testing methods based on micro- or nano-fabrication techniques are based on producing freestanding specimens directly integrated in a micro- or nano-testing platform processed by the same methods; (vii) several of the aforementioned methods have been combined in different ways, e.g. freestanding membranes or beams processed by lithography and etching methods (vi) are deflected by nanoindentor (i) or AFM (ii) or by a pressure (the so-called bulge test). In most cases, these methods have been adapted to work under different environmental conditions and range of temperatures with possible couplings to electrical or magnetic fields.

Some of the tested nano-sized systems can be produced with near-ideal defect-free microstructures or, alternatively, with extremely large densities of internal interfaces and defects. Among others, a number of elementary deformation mechanisms related to the nucleation, propagation, interactions and multiplication of defects can be experimentally revisited and quantitatively characterized through these new testing capabilities. Sometimes, unique mechanisms, related to unusual constraints associated to the small dimensions or to the nanocrystalline structure are unraveled, challenging the current state of knowledge, see, e.g., [5–10]. Furthermore, the level of stress and stress gradient that can be attained in some of these nanowire or thin-film-type systems being extremely large compared with bulk counterparts, due to the so-called "smaller is stronger" paradigm, significant distortion of the crystal lattice takes place, leading to strong modifications of the transport properties, involving for instance large piezoresistive, flexo-electric, or magnetostriction effects. The field of the so-called "strain engineering" in nano-objects reconciles and forces cross-fertilization between the mechanics of solids, materials science and solid-state physics communities in a way that perfectly corresponds to the legacy of Jacques Friedel, who always naturally conceived all these viewpoints within a unified approach. We had the opportunity to present and discuss with him a new concept for measuring experimentally the mechanical response of small-scale objects while allowing in situ defect characterization and transport measurements. The present contribution is an opportunity to explain the concept, to outline some recent extensions and results, and to indicate perspectives for its future development and expected contribution to the generation of new knowledge in this exciting field.

The outline of the paper is the following. The basic concept underlying the generic on-chip test method is presented in Section 2. Section 3 explains how the technique can be extended to address various loading, environmental and coupled effects, involving in situ capabilities. In Section 4, selected results obtained on Pd thin films over the last 4 years are revisited, involving interesting fundamental examples of dislocation and twin interaction mechanisms. Section 5 is devoted to the extraction of piezoresistance effects in silicon nanowires of different doping levels over a large range of deformations as an example of electrical–mechanical coupling analysis using this lab-on-chip test platform concept.

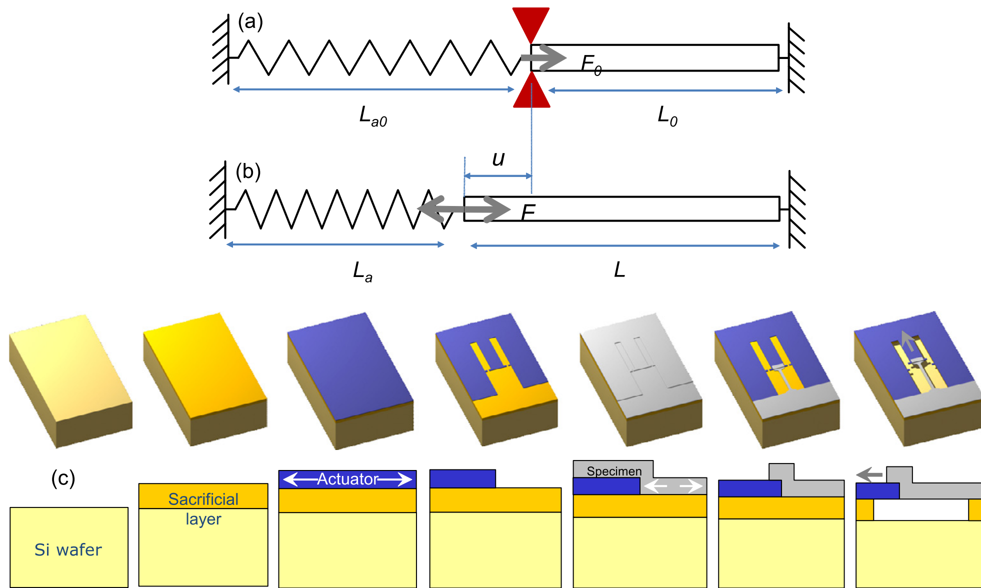

Fig. 1. Principle of an elementary uniaxial testing structure made of a preloaded actuating beam to which a long specimen is attached; (a)–(b) schematic illustration of the principle; (c) implementation into a microfabrication process.

2. The basic test concept

The inherent difficulty related to the manipulation of nano-sized objects, the damaging effect of ion-beam machining methods, and the need to apply very small loads and displacements in a controlled manner call for the development of test structures that are as simple as possible, with the minimum perturbation/contact with macroscopic instruments, and for light machining/etching recipes. Micro- and nano-fabrication methods (the example "vi" in the list provided in the introduction), originating from microelectronics processing approaches, involve robust and low-damage bottom-up techniques that allow producing very precise elementary patterns with a capacity to multiply them at will. Based on the former considerations, the most elementary generic test structure that allows deforming a material element up to large strains with minimum misalignment, and with minimum instrumentation and geometrical complexity is a long specimen of initial length L_0 attached to a preloaded spring of initial (deformed) length L_{a0}, see Fig. 1a. This spring undergoes a force F_0 and has a spring constant k. If the spring is allowed to relax, as in Fig. 1b, it then pulls on the test specimen until the equilibrium load F is attained, corresponding to a displacement u, with $F = F_0 - ku$. By knowing k, F_0, L_{a0}, and the specimen cross-section area A_0, the magnitude of the stress σ and of the strain ϵ (expressed here in terms of engineering stress and engineering strain) in the test specimen is entirely known as $\sigma = F/A$ and $\epsilon = u/L_0$ (assuming no initial force in the test specimen). There are two options to extract a full stress–strain response: either the spring is only progressively relaxed with a continuous measurement of u or multiple structures are used with different spring constants. The spring constant can be easily modified by changing the length of the spring, its cross-section or its constituent material.

This elementary test structure can be implemented in a number of ways using microfabrication methods. The most obvious way, represented in Fig. 1c, is by depositing and patterning, via lithography, long beams of one material (the so-called "actuator beam") followed by the deposition and patterning of the test specimen, with a sufficiently wide overlap between the two to ensure good adhesion. The two beams rest on a sacrificial layer, which can be etched away to release the "spring + specimen" structure. In order for the actuator beam to behave as a spring, different physical means can be used. One method is to deposit a material that contains high internal stress. This is the approach we have followed up to now through the use of silicon nitride (SiN) beams deposited by low-pressure chemical vapor deposition (LPCVD) with a consistent and reproducible internal stress near 1 GPa and no stress gradient that could lead to spurious distortion upon release [11–13]. The Young's modulus of SiN, which sets the spring constant k, is also quite reproducible. Other possible methods involve decreasing locally the temperature of the actuator beam to force thermal contraction, or to use a shape-memory alloy whose contraction upon phase transformation can be controlled by a small temperature change. The method based on internal stress built up during deposition is the most direct approach as it avoids any external means to impose the load. Furthermore, the displacement u can be measured by microscopy measurements avoiding also the use of a contacting instrument or sophisticated sensing devices; this is also the approach followed by Saif and co-workers, e.g., [14,15].

A full stress–strain response can only be built through testing many structures with different lengths in order to reach different deformation levels, see [12,13]. This means that a stress–strain curve is obtained through probing the response of several specimens, typically 25. On the one hand, this can be seen as a shortcoming, but, on the other hand, it provides

a statistical information on the dispersion from one specimen to another depending on the scatter observed in the curve. A true shortcoming of the method is that the measurement of the displacement is made some time after the loading has been applied, meaning that any short-term relaxation will not be measured. More details on the extraction of stress and strain, as well as on the uncertainty analysis can be found in Refs. [13,16]. The two most critical elements in the success of the method are the etching selectivity and the mechanical integrity of the overlap region. The etching selectivity must be very large to ensure that the actuator and sample dimensions are almost not affected and no material change/embrittlement occurs. The integrity of the overlap essentially involves adhesion problems and cracking issues due to the stress concentration and locally reduced thickness. These issues can be solved by introducing an adhesion layer a few nanometer thick at the overlap or by adding some true local reinforcement cap layers.

Note that other types of test structures based on bottom-up fabrication through deposition, lithography and etching steps have been proposed over the last 10 years [17–22], with more complex configurations than the one presented here, with the advantage of a continuous monitoring of the load and displacement during deformation. Some of these techniques require to bring a macroscopic instrument to the test frame in order to impose the load, for instance through a piezo- or electromechanical actuator, e.g., [17,18]. Other test structures are miniaturized tensile testing stages, consisting of true MEMS devices [19–22], which are very powerful approaches at the expense of simplicity in the fabrication process and with a need to perform delicate calibration procedures.

The elementary test structures described above have been successfully applied to a variety of systems over the last few years involving among others Si nanowires [23–25], polysilicon films [26], Al films [27], Pd films (see below) [28], and metallic glass films [29].

3. Extensions of the concept

The concept described above can be extended in many different ways summarized in Fig. 2:

- the geometry of the test specimens can be varied in many different ways, as long as the patterning remains in plane: notches, holes, cracks, slits or combinations of these can be introduced as shown in Fig. 2a, with typical dimensions around a few hundreds of nanometers with conventional photolithography or down to 10 nm by using e-beam lithography. In terms of dimensions, silicon nanowires with dimensions down to 20 nm width and thickness have already been tested [23–25]. There is no limit to the minimum thickness that can be tested, but for extremely small thickness the idea is to deposit the actuator after the specimen in order to minimize the risks of cracking at the overlap (but this option limits the choice of the actuator material in terms of deposition temperature because of the possible impact on the test material). Current efforts are made to test graphene with this technique;
- the loading configuration and geometry of the actuator can also be varied in order to impose shear, equibiaxial, crack opening, or multiaxial type loadings, see Fig. 2b. Furthermore, the actuator beam release rate can be controlled, hence the loading rate, by tapering of the actuator, see Fig. 2c. A double actuator made of two different materials can also be used with one material capable of small repeated fatigue displacement under the action of electrical impulses, see Fig. 2d;
- a major advantage of testing films and wires with thicknesses below 200 nm is the possibility to perform characterizations of crystal defects under stress by transmission electron microscopy (TEM) without any additional thinning process, see, e.g., [30]. The only difficulty is to perform the so-called back etching step in order to open a hole inside the Si wafer, see Fig. 2e. Note that additional characterization techniques can be used such as Raman spectroscopy [31] or vibration methods to evaluate the elastic strain in the specimen [32,33], or atomic force microscopy to monitor for instance the evolution of roughness under stress [34];
- relaxation/creep response of the test structures can be monitored after release by simply measuring the evolution of displacement with time [30,35,36];
- the test structures can easily be stored under various environmental conditions (temperature, moisture, gas, irradiation, etc.) before release to determine the impact on properties or after release to see the impact on relaxation. Current efforts are devoted to look at creep under irradiation in thin Cu films;
- Finally, the elementary test structures can be slightly complexified to allow coupled electromechanical or thermomechanical measurements (see also Section 5). Fig. 2f shows an example of a design that permits circulating an electric current under tensile loading conditions.

Not all the configurations shown in Fig. 2 have been fully developed yet, but proofs of concept have been achieved for almost all of them.

4. Selected results regarding elementary defect analysis in Pd films

The test method described in Section 2 involving some of the extensions presented in Section 3 has been recently applied to e-beam and sputter deposited Pd films. The films were deposited with thickness ranging from 80 to 500 nm. The microstructure, shown in Fig. 3, which is TEM micrograph on a transverse cross-section focused ion beam (FIB) prepared sample, involves columnar grains with ∼30 nm in plane grain size and a moderate density of nanotwins (∼25% of the grains

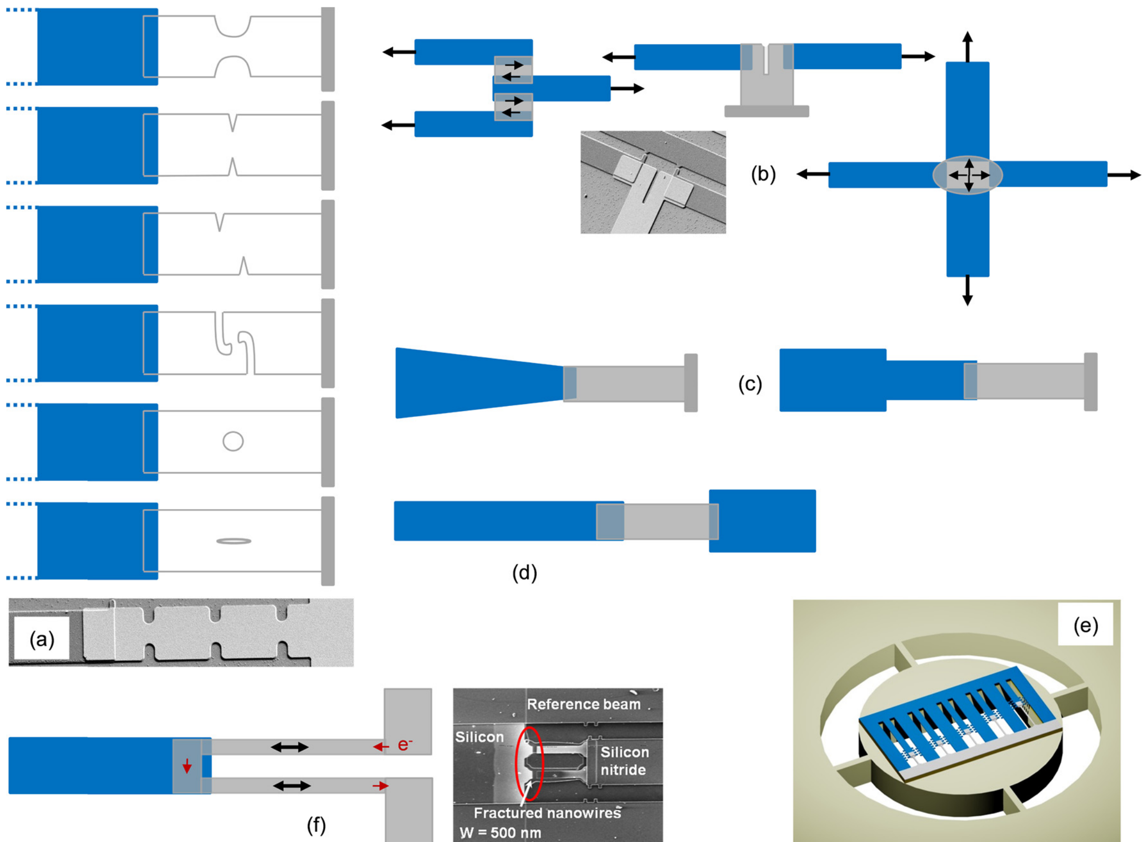

Fig. 2. Various extensions of the concept of internal-stress-driven mechanical loading, involving long actuator beams that contract upon release of the structure from the substrate through the etching of a sacrificial layer; (a) different patterns of the test specimen to create various local stress states and stress concentrations; (b) different arrangements of the actuator beams to induce different overall stress states; (c) different patterns of the actuator beams to control, by progressive release, the imposed displacement rate; (d) two actuator beams can be used with one made of piezo-electrically actuated material to impose displacement perturbations or small fatigue type loading cycle around the equilibrium position; (e) in situ TEM version with substrate back etching; (f) electrically coupled test specimens under uniaxial tension.

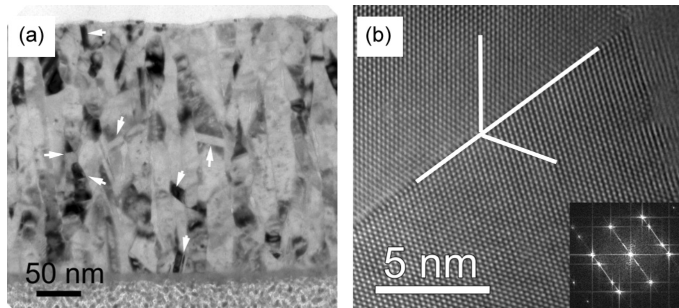

Fig. 3. (a) Bright field TEM micrograph obtained in an as-deposited 310-nm-thick Pd film. {111} growth twins indicated by white arrows can be seen. (b) HRTEM image of a single growth $\Sigma3\{111\}$ CTB.

contain one or more twins). TEM analyses have shown that the density of growth nanotwins depends on the deposition method and the resulting microstructure of the Pd films. The e-beam evaporated films involve randomly oriented nanograins with a relatively high density of growth twins, unexpected in view of the high stacking fault (SF) energy of Pd. In contrast, sputter-deposited films show a clear $\langle 111 \rangle$ crystallographic textured nanostructure without twins [37]. The formation of nanoscale growth twins in the non-textured e-beam evaporated Pd films can be attributed to the dissociation of high-energy grain boundaries (with large misorientation between the grains) into $\Sigma3\{111\}$ coherent twin boundaries (CTBs) and $\Sigma3\{112\}$ incoherent twin boundaries (ITBs) [38]. More recently, the influence of the deposition rate on the formation of growth twins in Pd films deposited by e-beam evaporation has been investigated using automatic crystallographic orientation mapping in TEM (ACOM-TEM) [39]. The statistical measurements demonstrated that the TB density and volume fraction of grains

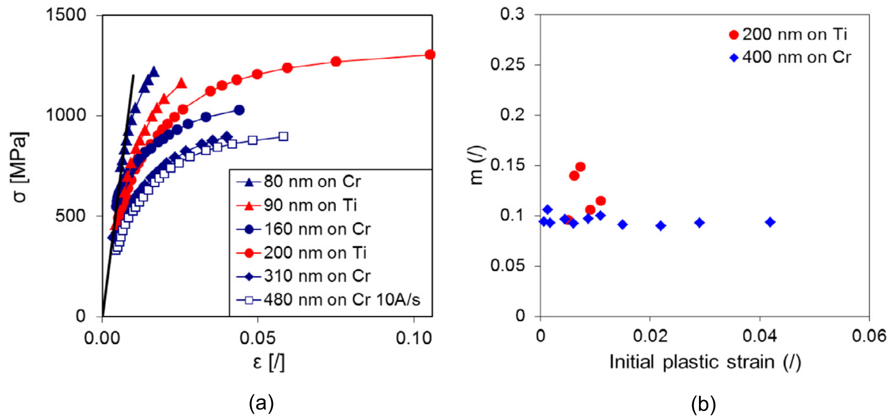

Fig. 4. Mechanical response of thin Pd films under uniaxial tension; (a) selection of true stress true strain curves for different film thicknesses deposited on a Ti layer (which is etched during the release) or a Cr layer (not etched during the release), (b) variation of the rate sensitivity index m.

containing twins increase with increasing the deposition rate. Furthermore, the analysis of the grain boundary character of different films shows that an increasing fraction of high-angle grain boundaries with misorientation angles around 55–65° leads to a higher potential for twin formation [39]. This indicates that, during atomic deposition, the formation of growth twins from high angle grain boundaries is favored as they provide higher driving forces for the formation of these twins.

The stress–strain responses of different Pd films obtained using the on-chip test structures and experimental protocols described in Section 2 are gathered in Fig. 4a, involving various thicknesses, two deposition rates (all films are deposited at a rate of 1 Å/s except one deposited at 10 Å/s) and the presence or not of a thin underlayer. As matter of fact, a thin (<5 nm) Cr or Ti layer had to be introduced to improve the adhesion of Pd on the SiN actuator over the overlap region. The etching selectivity was such that Cr was not etched away during the release, contrary to the Ti layer. The presence of one additional layer can have at least two possible effects. First, it can act as a barrier for dislocations to escape from the surface, such as a strong oxide layer; second it can break during deformation and create small pre-cracks that can deteriorate the ductility of the films. Note that the curves presented in Fig. 4a are reproducible when the tests are repeated and that the differences are representative of true effects. The uncertainty on the strain is small, below 3 to 5%, and this value decreases as the deformation gets larger because it essentially results from a fixed error in the measurement of the displacement (around 25 nm). The same comment applies to the estimation of the stress, but the starting error is larger as it is calculated from the subtraction of two quantities than can sometimes be relatively close to one another, i.e., in terms of the load, $F = F_0 - ku$ (see Section 2). In the present case of Pd beams, the error on the stress was estimated to be on the order of 10% and it decreases as the strain increases. The rate sensitivity has also been measured by looking at the evolution of the displacement with time. These measurements have been explained in detail in Ref. [30]. The approach relies on recording the evolution of the displacement with time, hence of the stress and strain in the specimen. From these data, the derivative of the strain with respect to time can be taken followed by the extraction of the variation of stress with strain rate. Fig. 4b shows the variations of the rate sensitivity index m (defined as $\partial \ln \sigma / \partial \ln \dot{\epsilon}$) averaged over the relaxation time for two different conditions as a function of the plastic strain attained after release. These values were confirmed by rate-dependent indentation tests. Additional effects of ageing or annealing before testing are not discussed here.

The main results that emerge from the analysis of the response of these films are the following:

(1) all films exhibit a high strain hardening capacity over several percent of plastic strain. The origin of this elevated strain hardening capacity comes from both kinematic (back stress) and isotropic contributions, but with a balance that cannot be determined without additional investigations. The result of this high strain hardening capacity is that high strength levels above 1 GPa are attained, which is remarkable for a pure FCC material;

(2) the strength increases with decreasing film thickness. This is the typical behavior in thin films, which is usually related to the fact that the grain size gets smaller when film thickness decreases. Here, as mentioned earlier, the in-plane grain size is always around 30 nm. Only the grain height varies. In Ref. [40], it was shown that the variation of grain height was sufficient to explain, using a relatively rudimentary homogenization model, the thickness effect.

(3) the rate sensitivity of the Pd films m typically varies between 0.03 and 0.15. These values are very high for FCC materials but in agreement with other data on nanocrystalline FCC metals [41–45]. The high rate sensitivity of nanocrystalline metals is related to the importance of the thermally activated phenomena showing up at small grain sizes and related to a deformation mode controlled by dislocation nucleation and/or grain boundary migration or sliding mechanisms (see later in this section). The corresponding activation volumes are typically between 2 and $20b^3$. Note that the activation volume tends to decrease when the plastic pre-strain imposed during the first fast loading increases and it increases with time (and thus with plastic relaxation), see [30]. These levels of activation volumes indicate that the mechanisms of deformation should be connected with dislocation mechanisms like nucleation or depinning from the very dense forests; see below. The variation with plastic strain is simply the result of a decrease in the activation volume as dislocations accumulate with plasticity,

giving rise to a decrease in the spacing between pinning points [30]. The same reasoning applies to relaxation, which leads to a decrease in the dislocation density with time;

(4) the absence of extra layer (when Ti is used as adhesion layer) has three effects. First, the thickness effect seems more limited than with the presence of a Cr layer, which indicates that the Cr capping layer plays a role on constraining the dislocations and preventing dislocation starvation. Secondly, the fracture strain is almost systematically (when looking at all the curves that have been measured) lower when a Cr layer is present. Thirdly, the rate sensitivity is higher in the absence of a capping layer during release (results not shown here, see [46]);

(5) the deposition rate seems to have a limited effect, but this conclusion is based only on two results obtained on films involving also two different thicknesses: 310 nm and 480 nm. A higher deposition rate leads to a higher density of twins. The tentative explanation for the similar strength observed in Fig. 4a is that the higher twin density of the thicker film compensates for the expected lower strength due to the higher thickness, but this should be confirmed with additional tests at similar thickness. The effect of the deposition rate seems more pronounced on the strain rate sensitivity: when deposited at higher rate, Pd relaxes a smaller amount of plastic strain under loading and stabilizes faster than when deposited at low rate, see [46];

(6) the ductility of the films is large compared with many other nanocrystalline systems, and this despite the large strength. This is reminiscent of the results obtained for nanotwinned Cu in the literature [47–49]. The mechanistic explanation relies on both the high strain hardening capacity and the high rate sensitivity, as well as presumably on the absence of significant defects. How these effects combine and cooperate to set the magnitude of the ductility has been recently addressed in Ref. [50]. In this reference, it is shown that the resistance to plastic localization is controlled by four main parameters – (i) the strain hardening exponent with a negative impact if it decreases (as predicted by the seminal Considère criterion), (ii) the rate sensitivity with a positive impact as it increases, (iii) the occurrence of so-called strain gradient plasticity effect, which can delay the development of necks, and (iv) the presence of imperfections, which can drastically decrease the resistance to localization. The presence of the Cr layer is assumed to produce small cracks upon deformation, which act as imperfections with a negative impact on ductility [51].

In order to understand the high strain hardening capacity leading to the good strength/ductility balance, as well as the origin of the rate sensitivity upon relaxation, different TEM and high-resolution (HR) TEM experiments have been performed to unravel the underlying physical mechanisms. Careful HRTEM analyses of as-deposited and deformed Pd films have shown a clear increase of the dislocation density within the grains, confirming that the Pd films deform by the intragranular activation of slip systems despite the small $\sim$30 nm grain size [28,52]. Furthermore, the dislocations interact with the growth nanotwins, leading to a progressive loss of coherency of $\Sigma 3\{111\}$ CTBs due to the accumulation of lattice dislocations at the TBs [28,52] as can be seen in the HRTEM images of Figs. 5a, 5b and 5c. Such a feature is also confirmed in the graph of Fig. 5d, showing an increase in the TBs thickness with increasing deformation. The term 'TBs thickness' is defined here as the distance separating the two last non-distorted twinning planes delimiting the matrix and the twinned region. The positions of these planes are indicated by dashed white lines in Figs. 5b and 5c, from which the inclined {111} planes, indicated by white solid lines, start to deviate from the initial position because of the accumulation of dislocations at the TBs (see [30] for more details). The loss of coherency of TBs is enhanced by the small grain size (i.e. nanoscale TBs accommodating a high dislocation density). In addition to demonstrating the capacity of TBs to increase dislocation storage in nanotwinned metals, these results prove that $\Sigma 3$ {111} CTBs can be used as markers for qualitative evaluation of the level of plastic deformation developed in individual grains [28,30,52]. Furthermore, detailed TEM analyses of TBs in Pd films deformed to moderate strain levels have shown that $\Sigma 3\{111\}$ CTBs offer multiple barriers to dislocation motion as well as sources for dislocation storage and multiplication providing an isotropic hardening contribution. Two major types of lattice dislocation/TB interactions have been revealed: the trapping of lattice dislocations with the creation of sessile Frank dislocations at the TB and the transmission of lattice dislocations via the TB. All these mechanisms involve twinning dislocations left along the TB [30].

More recently, the in situ extension of the on-chip method described in Section 3 has been used with HRTEM to directly observe the elementary defect mechanisms controlling the relaxation in $\langle 110\rangle$ textured Pd films with columnar microstructure [30]. The results revealed large creep/relaxation rates at room temperature during long periods of time, difficult to perform using classical methods for which stability of the electronics and thermal drift issues make long-term measurements inaccurate. The time-resolved HRTEM characterization of the evolution of the microstructure showed that, despite the small grain size, the creep/relaxation mechanism is mainly mediated by the stress-driven thermally activated nucleation and depinning of dislocations. During relaxation, the high dislocation density induced by the release of the film and the initial tensile force from the actuator decreases by a factor $\sim$2 to reach a steady-state level [30]. Such feature can be observed in Figs. 5e–f, in which the inverse fast Fourier transform (IFFT) images extracted from HRTEM images illustrate the dislocation activity during relaxation at exactly the same location over time. Interestingly, the formation and the destruction of sessile Lomer–Cottrell dislocations were observed in the time series [30] (a Lomer–Cottrell lock can be seen in Fig. 5f). Furthermore, a clear loss of coherency of CTBs with time evidenced by a progressive increase in the thickness of these boundaries in the HRTEM images was observed. This was attributed to the accumulation of lattice dislocations on CTBs during relaxation. GB-mediated mechanisms that often lead to a high-rate sensitivity of nanocrystalline materials have been excluded based on the analysis of grain size and crystallographic texture using ACOM-TEM as well as HRTEM. Such mechanisms can be avoided or, at least, mitigated, by the presence of a $\langle 110\rangle$ textured columnar microstructure in the Pd films.

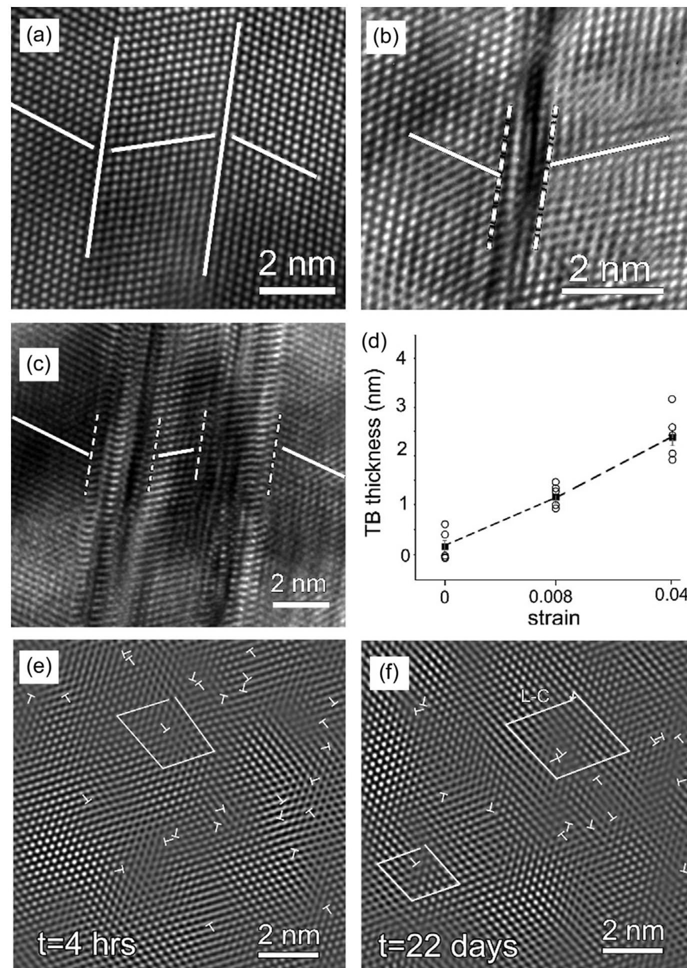

Fig. 5. HRTEM micrographs showing typical twin boundary structures in three different 310-nm-thick Pd specimens; (a) before deformation, (b) at $\varepsilon = 0.008$, and (c) at $\varepsilon = 0.04$; (d) evolution of the TB thickness in as-deposited and strained Pd films; note that some growth TBs exhibit small loss of coherency in the as-deposited films due to the internal stress developed during the deposition of the films; (e) and (f) filtered HRTEM micrographs showing the continuous change of the dislocation positions with time; note the formation of Lomer–Cottrell dislocations indicated by L–C in (f); the perfect dislocations are indicated by 'T' symbols.

Based on all these characterizations, some of the assumptions made in Ref. [51] to model the behavior of the Pd films with a simple homogenisation approach can now be challenged. Dislocation accumulation during plastic deformation is obvious, which means that one contribution to the strain hardening capacity comes from a forest-hardening-type mechanism, which was not accounted for in the proposed model [51]. This means that the impact of the twins on the strain hardening capacity was probably overestimated – as also concluded from the analysis of Fig. 4. Current work aims at modelling the films using a finite-element-based viscoplastic polycrystal plasticity model to also take into account the effects of heterogeneities and rate sensitivity.

Note that hydrogen absorption experiments in Pd films were recently performed in order to analyze the defects generated due to the extremely large stress building up during H loading. Unexpected defects not observed under uniaxial deformation have been revealed. Indeed, HRTEM analyses in Pd films subjected to hydriding cycles at high pressures revealed that growth $\Sigma 3\{112\}$ incoherent TBs dissociate after hydriding into two phase boundaries bounding a new and unstable 9R phase involving the formation of parallel single SFs located every three $\{111\}$ planes in the fcc Pd structure [38,53]. This interesting and seldom encountered category of phase transformation is connected with the influence of the H on the SF energy of Pd and the high compressive stresses building up during hydriding [38,53]. Also, a high density of shear-type stacking faults has been observed after hydriding of Pd films. Such defects were not observed in both as-deposited and deformed Pd films. Taking into account the high SF energy of Pd, this indicates a clear effect of H on the nucleation energy barriers of Shockley partial dislocations in Pd.

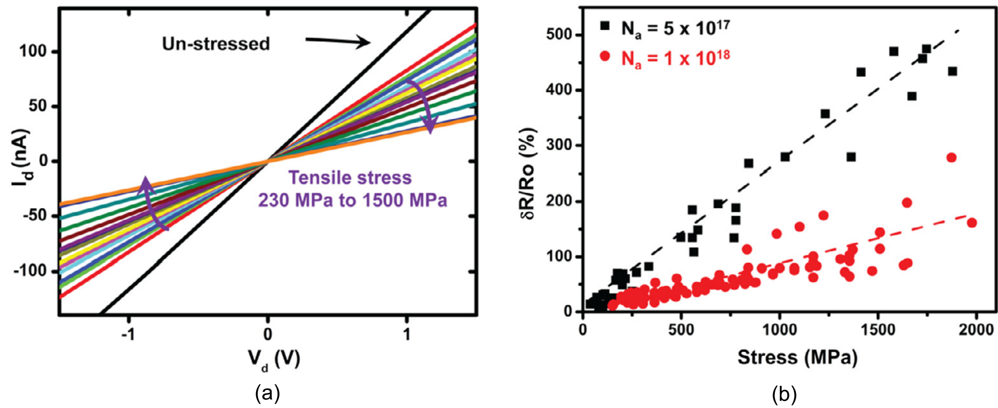

Fig. 6. (a) Output characteristics $I_d - V_d$ for a series of tensile test structures of 100-nm-thick, 2-μm-wide and 200-μm-long Si geometry with $N_a \sim 5 \cdot 10^{18}$ cm^{-3}; (b) normalized stress induced change in resistance ($\delta R/R_0$) for Si beams with $N_a \sim 1 \cdot 10^{18}$ and $N_a \sim 5 \cdot 10^{17}$ cm^{-3} as a function of the tensile stress.

5. Selected results regarding coupled mechanical–electrical effects

The piezo-resistance of 100-nm-thick, [110] oriented, p-type, mono-crystalline Si beams has been investigated under large uniaxial tension up to 2 GPa using the original on-chip tensile testing set-up described in Sections 2 and 3.

Piezo-resistance (π) is the change in resistance of a crystal upon elastic deformation. In Si, it primarily originates from a strain-induced alteration of the crystal symmetry and electronic band structure [54–57]. For example, the application of a uniaxial stress along the ⟨110⟩ direction reduces the original cubic crystal symmetry to orthorhombic symmetry [58]. This reduction of symmetry has a pronounced effect on the valence band edge, where the original degeneracy is lifted and split into two distinct heavy hole (HH) and light hole (LH) bands. There is also a significant warping of the energy bands away from the band edge. Since the inverse effective mass ($1/m*$) of the carriers is determined by the curvature of the band close to the band edge; the strain induced band splitting and warping influences the hole transport properties primarily through a change in $m*$ [58,59].

The π values for bulk Si have been extensively studied at low applied deformation, and shown to vary with orientation [54], impurity concentrations (N_a) [60], temperature [61] and with the magnitude of the loading [62,63]. However, these characterizations were primarily limited by the brittleness of Si exhibiting fracture stress below 300 MPa. Si nano-wires (SiNW) are promising candidates for the next generation of transistors [64]. It has been confirmed theoretically [65] and experimentally [66] that the strain-induced enhancement of mobility can be sustained in SiNW transistors. Additionally, the application of a deformation has the potential to tune SiNW properties as needed for electro-optic [67] and photo-voltaic [68] applications.

The piezo-resistive properties of Si nanostructures up to large elastic deformations have been explored using the on-chip test concept explained in Sections 2 and 3. The test structure design relies on a geometry made of two beams: a loop-shaped cantilever beam made of single crystal Si sharing a partial overlap with a stiffer cantilever beam of silicon-nitride (SiN) as illustrated in Fig. 2f [69]. More precisely, [110] oriented p-type Si nano-beams with N_a ranging from $1 \cdot 10^{16}$ to $1 \cdot 10^{19}$ cm^{-3} have been fabricated top down using 100-nm-thick Silicon-on-Insulator (SOI) wafers. The two silicon beams forming the loop have anchor pads that are isolated from one another. These regions are heavily p-doped for the realization of Ohmic contacts. An aluminum layer is deposited, on the silicon anchor pads and annealed to form the source and drain terminal. The HF release of the Si beams results in a high transient surface charge density $>10^{13}$ cm^{-2}. As a consequence, transport characterizations were made at least two weeks after the release to allow the dissipation of the transient surface charges and the regrowth of a stable native oxide, as reported in [70].

Fig. 6a plots the output characteristics ($I_d - V_d$) measured for an array of test structures with applied stress ranging from ~0.2 to 1.5 GPa. This specific structure is made of 100-nm-thick, 2-μm-wide and 200-μm-long Si beams with $N_a \sim 5 \cdot 10^{18}$ cm^{-3}. Fig. 6b compares the relative change of resistance ($\delta R/R_0$) as a function of the imposed stress extracted for $N_a \sim 1 \cdot 10^{18}$ and $\sim 5 \cdot 10^{17}$ cm^{-3}. The modulation of the resistance by a factor of 5.8 for $N_a \sim 5 \cdot 10^{17}$ cm^{-3} is significantly larger than the factor of ~4.5 predicted for hole-inversion layers [58]. In addition to the change in $m*$, there can also be contribution to δR originating from the modification of the carrier mean free path in the deformed crystal. In contrast to transport in the bulk of a Si crystal, where the effective carrier concentration p is a constant determined by N_a, in the case of Si thin films and SiNWs, p can be varied through the application of an electrostatic potential at the surface. Surface states [71] ensure that there is always an electrostatic potential at the surface. The extent of the resulting space charge region will, however, depends on N_a. A moderate positive surface charge density $N_{it} = 5 \cdot 10^{11}$ cm^{-2} at the native oxide interface would give rise to a total depletion region that would be over 10% and 50% of the Si film thickness for $N_a \sim 1 \cdot 10^{18}$ and $N_a \sim 5 \cdot 10^{17}$ cm^{-3}, respectively. This could be a reason for the enhanced influence of stress on π and R/R_0. Indeed, the stress-induced modulation of SiNW depletion length [72] is considered to cause the significant enhancement observed

by [73,74] in 'fully depleted' SiNWs. Several factors like the intensity of applied load, magnitude of enhancement (few folds in this study), and geometry (2-μm-wide beams) limit direct comparisons with the enhancement by two orders of magnitude reported for <100 nm-wide SiNWs [73] at very low applied stresses. The piezoresistance values are similar to the ones published by Milne [75] et al. and Koumela et al. [76] with the difference that the coefficients are extracted here over a much wider range of deformation, permitted by the large fracture stress of the SiNWs. More discussion about the piezoresistance effects in SiNWs are given in Ref. [77].

6. Conclusions

The conventional or more advanced micro- and nanofabrication methods used for microelectronics have been borrowed by the MEMS community to build over the last 20 years very sophisticated miniaturized devices with sensing and transducing capabilities. In the same vein, these same processing methods have been diverted from their original purpose by the materials science and physics communities to build a test platform for probing the properties of nanosized material specimens. These test platforms can go from very simple specimen support frames up to fully integrated multipurpose micro-scale testing machines. Here, we have described a suite of on-chip test structures with intermediate level of complexity that allow measuring the mechanical properties of very thin films or nanowires, with the possibility to address electrical or thermal couplings, under environmental conditions and with the potential for various in situ configurations. Two extreme types of applications have been described to demonstrate the interest of the method. The first application was on Pd films involving a high density of grain and twin boundaries, as well as high dislocation densities building up during deformation. The other system is an on-chip tensile testing setup allowing electro-mechanical characterization of 100 nm-thick Si beams and the extraction of the evolution of π and R/R_0 with N_a. The results suggest that significant strain-induced mobility enhancement could be potentially achieved for lowly-doped nano-scale semiconductor devices.

Acknowledgements

This research has been performed with the financial support of the "Politique scientifique fédérale" under the framework of the interuniversity attraction poles program, IAP7/21, as well as with the support of the "Communauté française de Belgique" under the program "Actions de recherche concertées" ARC 05/10-330 and ARC Convention No. 11/16-037. The support of the "Fonds belge pour la recherche dans l'industrie et l'agriculture (FRIA)" for M.-S. Colla is also gratefully acknowledged as are the FWO research projects G012012N "Understanding nanocrystalline mechanical behavior from structural investigations" for B. Amin-Ahmadi.

References

[1] K.J. Hemker, W.N. Sharpe Jr., Annu. Rev. Mater. Res. 37 (2007) 92.
[2] D. Gianola, C. Eberl, JOM 61 (2009) 24–35.
[3] Y. Lu, J. Lou, JOM 63 (2011) 35–42.
[4] M.F. Pantano, H.D. Espinosa, L. Pagnotta, J. Mech. Sci. Technol. 26 (2012) 545–561.
[5] J.R. Greer, J.T.M. De Hosson, Prog. Mater. Sci. 56 (2011) 654–724.
[6] K.S. Kumar, H. Van Swygenhoven, S. Suresh, Acta Mater. 51 (2003) 5743–5774.
[7] J. Rajagopalan, J.H. Han, M.T. Saif, Science 315 (2007) 1137580.
[8] O. Kraft, P.A. Gruber, R. Mönig, D. Weygand, Annu. Rev. Mater. Res. 40 (2010) 293–317.
[9] J.A. El-Awady, Nat. Commun. 6 (2015) 5926.
[10] F. Mompiou, M. Legros, M. Coulombier, J.-P. Raskin, T. Pardoen, Acta Mater. 61 (2013) 205–216.
[11] A. Boé, A. Safi, M. Coulombier, T. Pardoen, J.-P. Raskin, Thin Solid Films 518 (2009) 260.
[12] N. André, M. Coulombier, V. de Longueville, D. Fabrègue, T. Gets, S. Gravier, T. Pardoen, J.-P. Raskin, Microelectron. Eng. 84 (2007) 2714.
[13] S. Gravier, M. Coulombier, A. Safi, N. André, A. Boe, J.-P. Raskin, T. Pardoen, J. Microelectromech. Syst. 18 (2009) 555.
[14] M.A. Haque, M.T.A. Saif, Sens. Actuators 97–98 (2002) 239.
[15] M.A. Haque, M.T.A. Saif, Exp. Mech. 43 (2003) 248–255.
[16] R. Vayrette, J.-P. Raskin, T. Pardoen, Eng. Fract. Mech. (2015), http://dx.doi.org/10.1016/j.engfracmech.2015.07.006, in press.
[17] M.A. Haque, M.T.A. Saif, J. Microelectromech. Syst. 10 (2001) 146.
[18] M.A. Haque, M.T.A. Saif, Acta Mater. 51 (2003) 3053–3061.
[19] Y. Zhu, H.D. Espinosa, Proc. Natl. Acad. Sci. 102 (2005) 14503.
[20] H.D. Espinosa, Y. Zhu, N. Moldovan, J. Microelectromech. Syst. 16 (2007) 1219.
[21] P.O. Theillet, O.N. Pierron, Appl. Phys. Lett. 94 (2009) 181915.
[22] E. Hosseinian, O.N. Pierron, Nanoscale 5 (2013) 12532–12541.
[23] V. Passi, U. Bhaskar, T. Pardoen, U. Sodervall, B. Nilsson, G. Petersson, M. Hagberg, J.-P. Raskin, Rev. Sci. Instrum. 82 (2011) 116106.
[24] U. Bhaskar, V. Passi, S. Houri, E. Escobedo-Cousin, S.H. Olsen, T. Pardoen, J.-P. Raskin, J. Mater. Res. 27 (2012) 571.
[25] V. Passi, U. Bhaskar, T. Pardoen, U. Sodervall, B. Nilsson, G. Petersson, M. Hagberg, J.-P. Raskin, J. Microelectromech. Syst. 21 (2012) 822.
[26] S.S. Mulay, G. Becker, R. Vayrette, J.-P. Raskin, T. Pardoen, M. Galceran, S. Godet, L. Noels, Comput. Mech. 55 (2015) 73.
[27] M. Coulombier, A. Boe, C. Brugger, J.-P. Raskin, T. Pardoen, Scr. Mater. 62 (2010) 742.
[28] H. Idrissi, M.S. Colla, B. Wang, D. Schryvers, J.-P. Raskin, T. Pardoen, Adv. Mater. 23 (2011) 2119.
[29] M. Ghidelli, Size dependent mechanical behavior of Zr-Ni thin metallic glass films, Ph.D. dissertation, Université Catholique de Louvain, 2015.
[30] M.S. Colla, B. Amin-Ahmadi, H. Idrissi, L. Malet, S. Godet, J.-P. Raskin, D. Schryvers, T. Pardoen, Nat. Commun. 6 (2015) 5922.
[31] F. Ureña, S.H. Olsen, L. Siller, U. Bhaskar, T. Pardoen, J.-P. Raskin, J. Appl. Phys. 112 (2012) 114506.
[32] S. Houri, U. Bhaskar, B. Gallacher, L. Francis, T. Pardoen, J.-P. Raskin, Exp. Mech. 53 (3) (2013) 441.
[33] S. Houri, U.K. Bhaskar, T. Pardoen, J.-P. Raskin, Rev. Sci. Instrum. 84 (2013) 036102.

[34] E. Escobedo-Cousin, S.H. Olsen, T. Pardoen, U. Bhaskar, J.-P. Raskin, Appl. Phys. Lett. 99 (2011) 241906.
[35] M. Coulombier, G. Guisbiers, M.-S. Colla, J.-P. Raskin, T. Pardoen, Rev. Sci. Instrum. 83 (2012) 105004.
[36] G. Guisbiers, M.-S. Colla, M. Coulombier, J.-P. Raskin, T. Pardoen, J. Appl. Phys. 113 (2013) 024513.
[37] B. Wang, H. Idrissi, H. Shi, M.S. Colla, S. Michotte, J.-P. Raskin, T. Pardoen, D. Schryvers, Scr. Mater. 66 (2012) 866.
[38] H. Idrissi, B. Amin-Ahmadi, B. Wang, D. Schryvers, Phys. Status Solidi B 251 (2014) 1105.
[39] B. Amin-Ahmadi, H. Idrissi, M. Galceran, M.S. Colla, J.-P. Raskin, T. Pardoen, S. Godet, D. Schryvers, Thin Solid Films 539 (2013) 145.
[40] M.-S. Colla, B. Wang, H. Idrissi, N. Schryvers, J.-P. Raskin, T. Pardoen, Acta Mater. 60 (2012) 1795.
[41] Q. Wei, J. Mater. Sci. 42 (2007) 1709.
[42] M. Dao, L. Lu, R.J. Asaro, J.T.M. De Hosson, E. Ma, Acta Mater. 55 (2007) 4041.
[43] S. Cheng, E. Ma, Y.M. Wang, L.J. Kecskes, K.M. Youssef, C.C. Koch, U.P. Trociewitz, K. Han, Acta Mater. 53 (2005) 1521.
[44] Y.M. Wang, E. Ma, Acta Mater. 52 (2004) 1699.
[45] L. Lu, R. Schwaiger, Z.W. Shan, M. Dao, K. Lu, S. Suresh, Acta Mater. 53 (2005) 2169–2179.
[46] M.S. Colla, Plasticity and creep in thin free-standing nanocrystalline Pd films, Ph.D. dissertation, Université Catholique de Louvain, 2014.
[47] L. Lu, Y.F. Shen, X.H. Chen, L.H. Qian, K. Lu, Science 304 (2004) 422–426.
[48] M. Dao, L. Lu, Y.F. Shen, S. Suresh, Acta Mater. 5421 (2006) 5421–5432.
[49] Q.S. Pan, L. Lu, Acta Mater. 81 (2014) 248–257.
[50] T. Pardoen, J. Mech. Phys. Solids 62 (2014) 81–98.
[51] M.-S. Colla, B. Wang, H. Idrissi, N. Schryvers, J.-P. Raskin, T. Pardoen, Acta Mater. 60 (2012) 1795.
[52] B. Wang, H. Idrissi, M. Galceran, M.S. Colla, S. Turner, S. Hui, J.-P. Raskin, T. Pardoen, S. Godet, D. Schryvers, Int. J. Plast. 37 (2012) 140–156.
[53] B. Amin-Ahmadi, H. Idrissi, R. Delmelle, T. Pardoen, J. Proost, D. Schryvers, Appl. Phys. Lett. 102 (2013) 071911.
[54] C. Smith, Phys. Rev. 919 (1954).
[55] C. Herring, E. Vogt, Phys. Rev. 1 (1956).
[56] J. Bardeen, W. Shockley, Phys. Rev. 549 (1950).
[57] M.V. Fischetti, Z. Ren, P.M. Solomon, M. Yang, K. Rim, J. Appl. Phys. 94 (2003) 1079.
[58] Y. Sun, S.E. Thompson, T. Nishida, J. Appl. Phys. 101 (2007) 104503.
[59] M. Chu, Y. Sun, U. Aghoram, S.E. Thompson, Annu. Rev. Mater. Res. 39 (2009) 203.
[60] Y. Kanda, IEEE Trans. Electron Devices 29 (1982) 64.
[61] O. Tufte, E. Stelzer, Phys. Rev. (1964).
[62] K. Matsuda, Y. Suzuki, K. Kanda, J. Appl. Phys. 1838 (1993).
[63] J. Aubrey, W. Gubler, T. Henningsen, S. Koenig, Phys. Rev. 130 (1963).
[64] J.-P. Colinge, C.-W. Lee, A. Afzalian, N.D. Akhavan, R. Yan, I. Ferain, P. Razavi, B. O'Neill, A. Blake, M. White, A.-M. Kelleher, B. McCarthy, R. Murphy, Nat. Nanotechnol. 5 (2010) 225.
[65] Y.-M. Niquet, C. Delerue, C. Krzeminski, Nano Lett. 12 (2012) 3545.
[66] J.-P. Raskin, J.-P. Colinge, I. Ferain, A. Kranti, C.-W. Lee, N.D. Akhavan, R. Yan, P. Razavi, R. Yu, Appl. Phys. Lett. 97 (2010) 042114.
[67] R.S. Jacobsen, K.N. Andersen, P.I. Borel, J. Fage-Pedersen, L.H. Frandsen, O. Hansen, M. Kristensen, A.V. Lavrinenko, G. Moulin, H. Ou, C. Peucheret, B. Zsigri, A. Bjarklev, Nature 441 (2006) 199.
[68] Z. Wu, J.B. Neaton, J.C. Grossman, Nano Lett. 9 (2009) 2418.
[69] U.K. Bhaskar, V. Passi, S. Houri, E. Escobedo-Cousin, S.H. Olsen, T. Pardoen, J.-P. Raskin, J. Mater. Res. 27 (2011) 571.
[70] U.K. Bhaskar, V. Passi, T. Pardoen, J.-P. Raskin, J. Appl. Phys. 113 (2013) 13450.
[71] J. Bardeen, Phys. Rev. 71 (1947) 717.
[72] A.C.H. Rowe, Nat. Nanotechnol. 3 (2008) 311.
[73] R. He, P. Yang, Nat. Nanotechnol. 1 (2006) 42.
[74] P. Neuzil, C.C. Wong, J. Reboud, Nano Lett. 10 (2010) 1248.
[75] J.S. Mile, A.C.H. Rowe, S. Arscott, C. Renner, Phys. Rev. Lett. 105 (2010) 226802.
[76] D. Koumela, C. Mercier, G. Dupré, G. Jourdan, C. Marcoux, E. Ollier, S.T. Purcell, L. Duraffourg, Nanotechnology 22 (2011) 395701.
[77] U.K. Bhaskar, T. Pardoen, V. Passi, J.-P. Raskin, Appl. Phys. Lett. 102 (2013) 031911.